PCCP

Accepted Manuscript

ROYAL SOCIETY OF CHEMISTRY

www.rsc.org/pccp

Geometric and electronic structure and magnetic properties of Fe-Au nanoalloys: insights from *ab initio* calculations

Sampyo Hong[a,b] and Talat S. Rahman[a,*]

[a] Department of Physics, University of Central Florida, Orlando, FL 32816
[b] Department of Physics, University of North Florida, Jacksonville, FL 32224

*Corresponding author. Email: talat.rahman@ucf.edu.

Abstract

We have performed density functional theory (DFT) based calculations of Fe-Au nanoalloys containing 113 atoms, Fe_xAu_{113-x} (x=23, 56, 90), to determine their preferred geometric structure and the ensuing electronic structural and magnetic properties. We find that these nanoalloys prefer the formation of core-shell structure and the Fe core maintains almost constant magnetic moment of ~2.8 μ_B regardless of the Fe content, which is 27% enhancement from the bulk value and in qualitative agreement with some previous results. The local magnetic moment of Fe atoms are well correlated with the local coordination of the Fe atoms. Furthermore, the enhancement of the magnetic moment may be traced to charge depletion from the Fe atoms in the core to the Au atoms in the shell. The preference for the core-shell structure over one with segregated Fe and Au parts could be the low surface tension at the Fe-Au interface, which is larger for the core-shell structure, and can be attributed to strong Fe-Au interfacial interaction as a result of large charge transfer at the interface.

1. Introduction

Magnetic nanoparticles are of considerable interest for many applications that require small particles with high magnetic susceptibility, as these they provide excellent interaction with external magnetic fields. Their application in biomedicine is also large.[1-3] Also, if they are coated by a noble metal such as gold, they could be further functionalized while being protected from oxidation. For example, gold coating can prevent corrosion of iron and enable thiol groups to bind to the surface, which is otherwise difficult to achieve. Furthermore, since gold nanoparticles are good catalysts and optically active, gold-coated Fe nanoparticles may possess enhanced optical and catalytic activity.[4,5] Thus gold-coated Fe nanoparticles of high magnetic susceptibility benefit from synergistic effects that could make them suitable for both biomedical and catalytic applications. However, there exist difficulties associated not only with the fabrication of gold-coated Fe nanoparticles of specific size, composition and geometry, but also in their

characterization.[6] There are also questions about oxidation state of the Fe atoms in this nanoalloy[7]. Notwithstanding the fact that bulk Fe and Au do not form an alloy rather show strong segregation[8], there may be miscibility issues between Fe and Au in the nanoalloy, since at the nanoscale properties may be different from that for the bulk material[9].

Despite the challenges, insightful results about Fe-Au nanoalloys have been reported.[10-21] For example, Fe-Au thin films and nanoparticles were observed to have bcc structure at high Fe content and fcc structure at low Fe content[5,10]. Icosahedral geometry was also suggested for 11% Fe content[17]. Formation of Fe-Au alloy was indicated for Fe content of 50% or higher, whereas a mixture of segregated Fe and Fe-Au alloy phases was indicated for Fe content of 20%.[19,20] At least for Fe-Au alloy with 20% Fe content the formation of Fe-core/Au-shell structure was suggested.[19] At 1073K, regardless of Fe content (>20%), segregation of Au atoms to surface occurred.[19] The magnetic moment of thin Fe-Au film was found to be constant almost independent of Fe content (2.2 μ_B per Fe over the range of 26 – 92% Fe) in one set of experiments.[10] Other experiments reported ~3 μ_B per Fe.[11,22] At the Fe-Au interface the magnetic moment of Au-Fe-Ag thin film is observed to be 2.6 μ_B.[18] For Au-Fe bulk alloy, long range ordering was ferromagnetic for Fe content > 15% and below 40K, and antiferromagnetic for lower Fe content leading to spin glass behavior.[12] This spin glass behavior in Au rich Fe-Au alloys was attributed to magnetic frustration caused by competition of antiferromagnetic and ferromagnetic interactions[15]. On the theoretical side, a density functional theory (DFT) based study of Fe-Au nanoparticles of fixed geometry (Fe_xAu_y, x=1,13, y=12,42,54,134) in which the 1- and 13-atom Fe cores were caged in icosahedral Au shell, showed a magnetic moment of ~ 2.9 μ_B per Fe atom, irrespective of the Au content, in agreement with experiment.[16] To our knowledge, little theoretical attention has been paid to Fe-Au nanoalloys of varying structure and any other composition.

Here, we present DFT results for the structural and magnetic properties of the 113-atom Fe-Au nanoparticles Fe_xAu_{113-x} (x=23, 56, 90), i.e. with Fe content of approximately 20%, 50% and 80%. Among a set of isomers with core-shell or non-core-shell geometry for each of these nanoalloys, we find a consistent trend that it is energetically favorable for Au atoms to occupy the shell and Fe atoms the inner core, thereby attesting that at least at very low temperatures, these Fe-Au nanoparticles form core-shell structure. Furthermore, we find that these core-shell nanoparticles have an almost constant magnetic moment of ~2.8 μ_B, significantly higher than that of bulk iron (2.2 μ_B), in agreement with previous studies, and that the magnetic moment of the core Fe atoms correlates with both Fe-Fe coordination and Fe oxidation state.

2. Theoretical Methods

Density functional theory (DFT)[23,24] calculations were performed using the Vienna *ab initio* simulation package (VASP)[25-27] employing the projector augmented wave (PAW) method[28]. Exchange-correlation energy is included in the calculation using the Perdew-Burke-Enzerhof functional.[29] Calculations were performed using 268 eV as the plane-wave energy cut-off. A supercell of dimensions 25Å x 25Å x 25Å was used to simulate bimetallic Fe_xAu_{113-x} (x=23, 56, 90) nanoparticles, which have the size of about 1.3 nm in diameter. The chosen size (113 atoms) was a compromise between computational tractability and physical-soundness of the model, as it is a geometric magic number for a bcc crystal. It is sufficiently large so as to provide a sizeable bulk-like core (~ 23 atoms in the minimum) as well as a shell thickness (~ 23 atoms in the minimum) representative of a core-shell nanoparticle. There was a vacuum space about 12Å between the nanoparticles and their periodic images. Because of the large size of the supercell, a single k-point was sufficient for sampling the Brillouin zone. We used a Fermi-level smearing of 0.2 eV. The threshold for electronic energy convergence was set to $1x10^{-4}$ eV, and that for structural optimization to 5×10^{-2} eV/Å. The ionic cores of all atoms in the Fe_xAu_{113-x} and Fe_x (x=23,113) nanoparticles were allowed to relax freely to their equilibrium position before ascertaining their electronic and geometric properties.

Prior to the molecular static DFT relaxations, classical molecular dynamic (MD) simulations were performed using the LAMMPS code[30] to generate initial geometries (candidate isomers) of the Fe-Au and Fe nanoparticles of interest using empirical embedded atom method potentials,[31] by annealing the nanoparticles from 300 K to 1000 K in a run of about 1 ns. Overall, the embedded atom method potential generated similar ordering of the candidate nanoparticles as that from DFT calculations, although the energetic difference among the isomers was quite different. The initial *seed* geometries of the five types of nanoparticle (Fe_xAu_{113-x} (x=23, 56, 90) and Fe_x (x=23,113)) for the classical molecular dynamics simulations were derived from the bulk bcc structure. With the isomer structures obtained from classical MD simulations, we performed *ab initio* molecular dynamics simulations using the more accurate first-principles pseudopotentials, for the same temperature range and for about 1000 MD steps.[25-27] Since isomers with core shell geometry were not automatically produced from these MD simulations, we created them by manually moving Au atoms from inside the nanoparticles to their surface. Thus, we had a pool of isomers with core-shell and non-core-shell geometry for each of the five types of nanoalloys of interest. Finally, these geometries were fully relaxed in the static DFT calculations to determine the energetic order of the isomers. The angular-momentum-decomposed, local density of states of the Fe-Au nanoparticles were calculated by projecting the wave function into the PAW volumes centered at each Fe

and Au atom. To calculate atomic charges we performed Bader charge analysis using a fine Fast Fourier Transform grid (192 x 192 x 192).[32,33] Furthermore, the local magnetic moments of Fe and Au atoms were obtained by integrating the spin-polarized charge density over the Bader volumes. Thus obtained magnetic moments differed from the ones obtained using the PAW volumes by no more than 0.1 μ_B.

3. Results and discussion

a. Lowest energy structures of nanoalloy Fe_xAu_{113-x} (x=23, 56, 90)

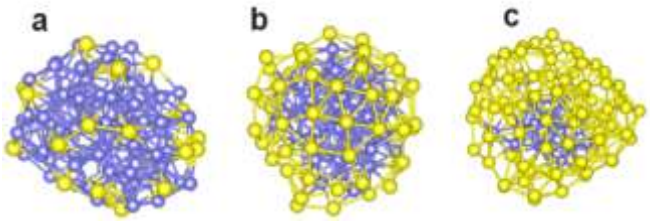

Figure 1. Most stable geometries of Fe_xAu_{113-x} nanoparticles: (a) x=90, (b) x= 56, and (c) x=23.

Figure 1 shows the calculated lowest energy structures of the Fe_xAu_{113-x} (x=23, 56, 90) nanoalloys obtained through the procedures described in the previous section. The corresponding Fe cores are shown in Fig. 2. Additionally, Figures 2d and 2e present the structure of the Fe_{23} and Fe_{113} nanoparticles (obtained through the same procedures). The internal structure of the Fe-Au nanoparticles (Fig. 2) varies with their Fe content and displays considerable disruption from the orderly arrangement of the corresponding pure Fe nanoparticles. For example, Fe_{113} (Fig. 2d) surfaces display predominantly triangular facets, and thus are similar to the (110) surfaces of the bcc crystal. To highlight the contrast in the structure of the pure Fe and Fe-Au nanoparticles, we present in Fig. 3 the distribution of the coordination numbers (i.e. the number of the 1st nearest neighbors) of Fe atoms in nanoparticles displayed in Fig. 2.

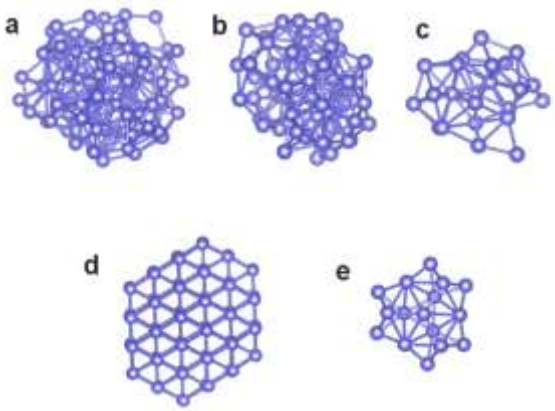

Figure 2. The geometry of the Fe cores of Fe_xAu_{113-x} for (a) x= 90, (b) x= 56, and (c) x=23; and that of pure (d) Fe_{113} and (e) Fe_{23} nanoparticles.

Fe_{113} shows the narrowest distribution among the nanoparticles indicating more organized structure than the others. It has peaks at coordination numbers of 7 and 8, the latter being a characteristic of bcc structure. As Au (Fe) content increases (decreases), the portion of the Fe atoms that have coordination of 8 decreases sharply and the distribution spreads to both lower and higher coordination numbers but with more weight on the former. Specifically, the center of the distribution changes from 6.3 for Fe_{113} to 6.8 for $Fe_{90}Au_{23}$, to 6.9 for $Fe_{56}Au_{57}$, to 5.7 for $Fe_{23}Au_{90}$. Table 1 contains structural parameters for these nanoparticles. The average 1st nearest neighbor Fe-Fe distance, d(Fe-Fe), of the nanoalloys is more or less the same, almost insensitive to the Fe content. Therefore, the decrease of the number of the 1st nearest neighbor of the Fe-Au nanoparticles for lower Fe content is a result of the increased disorder of the Fe core structure. For example, the core (Fe_{23}) of the $Fe_{23}Au_{90}$ nanoparticle is more disordered than the pure Fe_{23}, as clearly seen in Figs. 2 and 3. On the other hand, the increase in the Au-Au coordination as a function of Au content (Table 1) is related to the increased Au layer thickness. The Au shell becomes single-atom thick for Au content > 50% (Figs. 1b and 1c) and predominantly exposes the (111) facets, a feature of Au(111) surface in agreement with experiment[5,34]. Lastly, the development of the structure of the Au overlayer exhibited sequentially in Figs. 1a – 1c may show a possible route for the formation of the Au shell.

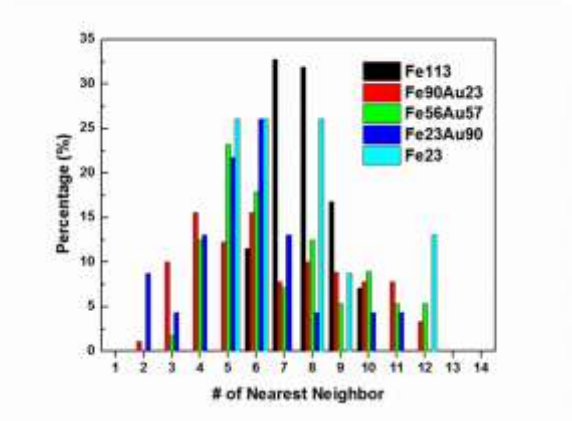

Figure 3. The distribution of 1st Fe-Fe nearest neighbors in the cores of Fe_xAu_{113-x} (x=23, 56, 90) nanoalloys and Fe_{113} and Fe_{23}. Only Fe atoms were considered in the calculation of the number of the nearest neighbors.

Table 1. Structural parameters of Fe_xAu_{113-x} (x=23, 56, 90) and pure Fe_x (x=23, 113). The cutoff distance for the 1st nearest neighbor (NN) interaction was 2.71Å for Fe-Fe bond length, and 3.0 Å for Fe-Au and Au-Au bond lengths.

	dFe-Fe (Å)	dFe-Au (Å)	dAu-Au (Å)	NN (Fe-Fe)	NN (Fe-Au)	NN(Au-Fe)	NN(Au-Au)
$Fe_{90}Au_{23}$	**2.50**	**2.72**	**2.90**	**6.8**	**1.5**	**6.0**	**0.4**
$Fe_{56}Au_{57}$	**2.52**	**2.73**	**2.85**	**6.9**	**3.0**	**2.9**	**3.2**
$Fe_{23}Au_{90}$	**2.52**	**2.85**	**2.84**	**5.7**	**4.3**	**1.1**	**5.5**
Fe_{23}	**2.49**	**-**	**-**	**7.3**	**-**	**-**	**-**
Fe_{113}	**2.45**	**-**	**-**	**6.3**	**-**	**-**	**-**

b. Formation of core-shell structure

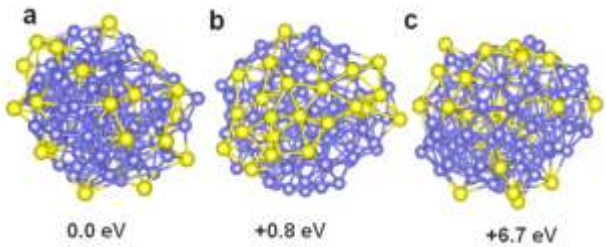

Figure 4. Isomers of $Fe_{90}Au_{23}$ nanoparticle.

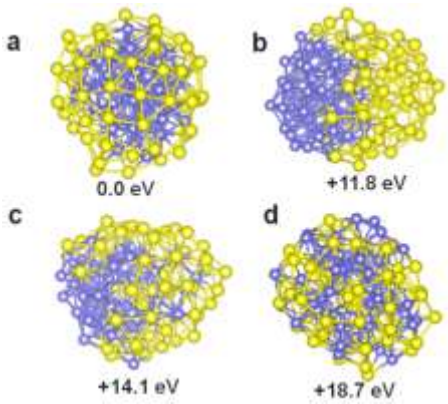

Figure 5. Isomers of $Fe_{56}Au_{57}$.

To affirm the formation of core-shell geometry for the three Fe-Au nanoalloys investigated here, albeit only a partial Au shell formation in $Fe_{90}Au_{23}$ owing to insufficient number of Au atoms (Fig. 1), we display in Fig. 4 the stable isomers of $Fe_{90}Au_{23}$. Initially, all 23 Au atoms were placed in the center of the nanoparticle. Even for classical and *ab initio* molecular dynamics simulations at a low temperature of 500K, Au atoms started to diffuse out of the central region and as temperature increased to 800K a majority of the Au atoms were found at the surface of the nanoparticle. A few of them, however, were remained inside core even at 800K as can be seen in Fig. 4c. However, when the inner Au atoms (in Fig. 4c) are manually placed on the shell and the nanoparticle configuration relaxed, these Au atoms rise to the surface and take up the structure shown in Fig. 4a, which is more stable than that in Fig. 4c. Interestingly, further classical molecular dynamic simulations using the geometry in Fig. 4a predict Au clustering on the surface of the nanoparticle (Fig. 4b). Incidentally, static DFT calculations predict the geometry in Fig. 4b, in which Au clustering occurs, to be less stable than the geometry in Fig. 4a (by a narrow margin of 0.8 eV). As will be discussed later, this disfavoring of Au clustering on the surface may be a result of charge transfer induced repulsion between the Au atoms.

The instability of the $Fe_{90}Au_{23}$ when it takes the structure of Au-core and Fe-shell is in marked contrast to the stability displayed by the inverse nanoparticle ($Fe_{23}Au_{90}$), when its core is Fe_{23} and the shell is Au_{90}, as found by our *ab initio* molecular dynamic simulations. Even at 1000 K we did not find its structure to deviate from that with a Fe-core and Au-shell. (The calculated cohesive energy of Fe_{113} and Fe bulk is 3.99 and 4.8 eV, respectively.) The Fe atoms simply remained inside and, more importantly, the Fe core was intact having no broken Fe-Fe bonds, indicating the stability of the core-shell structure. Note that the Fe core is not symmetric around the center of the nanoparticle. Rather, it is asymmetrically distributed off the center possibly owing to strain relief, as has been suggested.[35-37]

We find a similar trend for the $Fe_{56}Au_{57}$ isomers displayed in Fig. 5. The energetic order of the isomers of $Fe_{56}Au_{57}$ is opposite to their mixing order: the most alloyed isomer (Fig. 5d) is the most unstable. A less mixed Fe-Au geometry (Fig. 5c), in which most Au atoms are displaced out of the central region, is already more stable than that one in Fig. 5d by more than 4 eV. A more stable isomer (Fig. 5b) exhibits phase separation into two (coupled) Fe and Au clusters. In this geometry (Fig. 5b), a distinct interface develops between the Fe and Au clusters. However, the most stable isomer among them has the core-shell structure (Fig. 5a), in which all Au atoms are located on the surface of the nanoparticle and forms the overlayer uniformly covering the surface of the Fe core.

Regarding the driving force for segregation, several factors such as negative heat of solution, large surface energy and atomic size-mismatch, and core stress relief have been discussed in the literature.[8,37-40] On the one hand, surface energy of Au(111) (1.50 J/m^2)[41] is lower than that of Fe(110) (2.48 J/m^2)[41] and this large surface energy difference seems to be the major driving force for the segregation. On the other hand, considering the large difference in the bulk lattice constants of Fe and Au, relief of the resulting core-stress could also be forcing the Au atoms to move out of the core region.[19] In fact, our calculated 1st NN Au-Au bond length of Au_{23} and Au_{113} nanoparticles, in the range of 2.80 and 2.85 Å, is longer than Fe-Fe bond lengths (2.45 – 2.52 Å in Table 1) by 11-14%. An appreciable compressive stress at the Au-Fe interface induced by the surrounding Fe atoms is expected to be relieved when the Au atoms occupy the shell region, where the Au-Au bond length is about 2.85 Å (Table 1). However, the above mechanisms do not explain the preference of the Fe_xAu_{113-x} nanoparticles for the formation of core-shell structure over segregation into two independent Fe and Au clusters. For example, $Fe_{56}Au_{57}$ strongly favors the formation of core-shell structure over segregation into two Fe and Au clusters (compare Fig. 5a and 5b). Note that in the core-shell geometry in Fig. 5a, Au atoms uniformly cover (or wet) the surface of the Fe cluster and thus form a complete overlayer (or shell). A similar uniform distribution over the Fe surface occurs in the stable isomer of $Fe_{90}Au_{23}$ in Fig. 4a (although the energy difference is only 0.8 eV). The wetting of the Fe surface by the Au atoms indicates low surface tension at the Fe-Au interface, i.e., strong coupling between Fe and Au atoms at the interface. Furthermore, the structure in Fig. 5a has a larger interface than the segregated one in Fig. 5b. Considering that low surface tension at the interface induces large contact area, an important factor for the formation of core-shell nanoparticle in bi-metallic nanoparticles may be *low surface tension at the interface of two metallic species*.

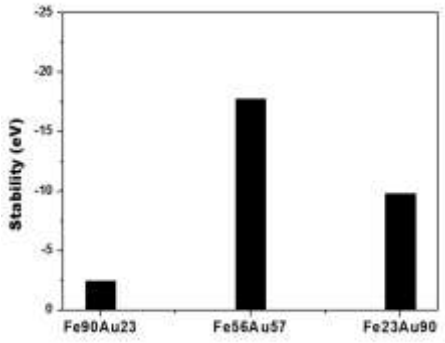

Figure 6. Relative stability defined as $E[Fe_xAu_{113-x}]-(x*E[Fe_{113}]+(1-x)*E[Au_{113}])$.

In order to estimate the stability of the formation of the core-shell structure, we introduce a parameter called relative stability, which is defined as $E[Fe_xAu_{113-x}]-(x*E[Fe_{113}]+(1-x)*E[Au_{113}])$ where x is the ratio of Fe to Au atoms in the cluster. This parameter provides an estimate of the energy gain of the core-shell structure with respect to the segregated phase consisting of two independent clusters of $x*Fe_{113}$ and $(1-x)*Au_{113}$. The hypothesis behind the concept is that when the decomposition of the core-shell nanoparticles happens, the decomposed Fe and Au atoms would form a part of Fe_{113} and a part of Au_{113} clusters, respectively. A positive value of this parameter indicates that the cluster is unstable and would undergo decomposition into $x*Fe_{113}$ and $(1-x)*Au_{113}$ clusters. From the calculated values for Fe_xAu_{113-x} nanoparticles shown in Fig. 6, we infer that $Fe_{56}Au_{57}$ and $Fe_{23}Au_{90}$ are stable by a substantial energy margin, while $Fe_{90}Au_{23}$ is marginally stable, suggesting possible propensity of $Fe_{90}Au_{23}$ to segregate. Recall that $Fe_{56}Au_{57}$ and $Fe_{23}Au_{90}$ nanoparticles have the core-shell structure with Au atoms forming a complete (closed) overlayer. In contrast, $Fe_{90}Au_{23}$ has an open, incomplete, core-shell structure and thus seems to be prone to segregation, possibly at elevated temperature. Thus, we attribute the stability of the former nanoparticles to the completeness of the core-shell structure, i.e., to enhanced interfacial interaction.

c. Oxidation state of Fe and Au atoms of bimetallic Fe_xAu_{113-x} (x=23, 56, 90)

Figure 7 shows the oxidation state of Fe and Au atoms in Fe_xAu_{113-x} nanoparticles. Here, the oxidation state was calculated by subtracting the number of electrons of each atom in the Fe_xAu_{113-x} nanoparticles from the number of electron of the corresponding neutral atom. Thus, positive (negative) oxidation state means electron loss (gain) and thus positive (negative) charging. Each symbol in Fig. 7 represents each atom in the nanoparticles. Therefore, the distribution of oxidation states for 1st nearest neighbor Fe-Fe coordination numbers in Fig. 7 represent the variation of the oxidation state of atoms in the specified nanoparticle depending on the local environment. All but 7 Fe atoms in $Fe_{56}Au_{57}$, and all but one Fe atom in $Fe_{23}Au_{90}$, and six Fe atoms in $Fe_{90}Au_{23}$ are positively charged (Fig. 7a). All of the negatively charged Fe atoms in $Fe_{56}Au_{57}$ and $Fe_{23}Au_{90}$ are located inside the Fe core and have the Fe coordination of 10 or higher and the Au coordination of either 0 or 1. Similarly, the six negatively charged Fe atoms in $Fe_{90}Au_{23}$ also have the Fe coordination of 8 or higher and at the same time Au coordination of zero or 1 and are all located inside the nanoparticle, and not at its surface. However, since not all of the Fe atoms in $Fe_{90}Au_{23}$

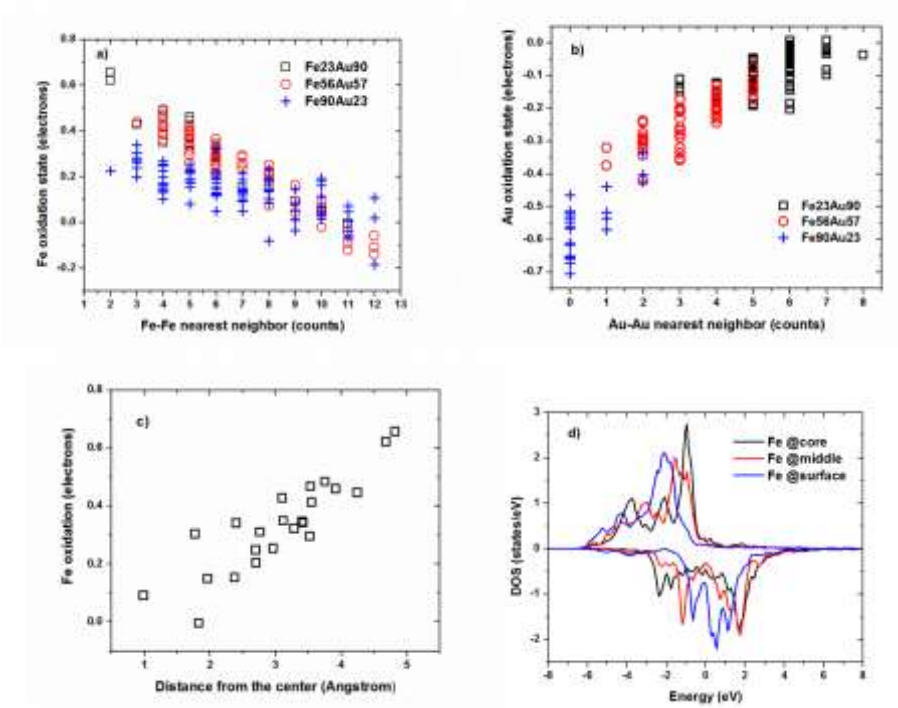

Figure 7. (a) The distribution of the oxidation state of the Fe atoms in the Fe_xAu_{113-x} (x=23,56,90) nanoparticles with respect to the number of the Fe-Fe 1st nearest neighbors (only Fe atoms within the 1st nearest neighbor are counted); (b) The distribution of the oxidation state of the Au atoms in the Fe_xAu_{113-x} (x=23,56,90) nanoparticles with respect to the number of the Au-Au 1st nearest neighbors (only Au atoms within the 1st nearest neighbor are counted); (c) the oxidation state of Fe atoms in the $Fe_{23}Au_{90}$ nanoparticle as the function of the distance from the center of the nanoparticle; and (d) the density of states of an Fe atom at the core, in the middle, and at the Fe-Au interface of the $Fe_{23}Au_{90}$ nanoparticle.

that have high Fe and low Au coordination (zero or 1) are negatively charged, the condition of high Fe coordination and/or zero or 1 Au coordination is a necessary but not a sufficient condition for negative oxidation state, depending on the details of the local environment.

In comparison, all *Au* atoms in $Fe_{90}Au_{23}$ and $Fe_{56}Au_{57}$ and all except two Au atoms in $Fe_{23}Au_{90}$ are negatively charged (Fig. 7b). The two positively charged Au atoms in $Fe_{23}Au_{90}$ have *Au* coordination of 6 or 7 and Fe coordination of zero or 1. The overall trend described above indicates a net charge transfer from the Fe core to the Au shell. In fact, Bader analysis of the atomic charge for the Fe-Au nanoparticles shows that the net charge transfer from the Fe core to the Au shell happens to be 7.68 electrons for $Fe_{23}Au_{90}$, 13.39 electrons for $Fe_{56}Au_{57}$, and 12.53 electrons for $Fe_{90}Au_{23}$. This leads to the average oxidation state of Fe atom to be 0.33 for $Fe_{23}Au_{90}$, 0.06 for $Fe_{56}Au_{57}$, and 0.13 for $Fe_{90}Au_{23}$. For Au atom the values are -0.08 for $Fe_{23}Au_{90}$, -0.23 for $Fe_{56}Au_{57}$, and -0.54 for $Fe_{90}Au_{23}$. Thus, there is a trend that smaller ratio of Au/Fe atoms in the nanoalloy leads to larger charge gain by the Au atoms. On the one hand, the electrostatic repulsive interaction between the Au atoms, particularly in $Fe_{90}Au_{23}$ causes uniform distribution of the Au atoms on the surface of the nanoparticle. On the other hand, the substantial charge transfer from the Fe to the Au atoms indicates strong interaction (binding) between the two species at the interface. This interaction must be a cause for the low surface tension at the interface, for example for $Fe_{56}Au_{57}$ nanoparticle, which leads to the formation of the overlayer/shell structure at the interface.

The oxidation state of the Fe atoms in the Fe-Au nanoparticles also depends on the distance from the center of the nanoparticle (Fig. 7c). The closer the Fe atom is to the surface, the higher is its oxidation state. This is a result of the increased Au coordination of the Fe atom in the proximity of the Au shell and subsequent charge transfer from the Fe atom to the neighboring Au atoms. The density of states of the d orbitals of an Fe atom (in Fig. 7d) show that the spin-up states of an Fe atom located closer to the shell undergoes larger blue shift, whereas the spin-down states undergo larger red shift than those of an Fe atom located farther to the shell. Therefore, when an Fe atom sits closer to the shell the spin-up states are more occupied but the spin-down states are less occupied. Moreover, the relative strength of the red shift of the spin-down states are larger than that of the blue shift of the spin-up states, resulting in the increase of net oxidation state of the Fe atom (Fig. 7d).

As described above, the core-shell Fe-Au nanoparticles (in Fig. 1) have a positive-core and negative-shell structure, which is similar to that of atomic nucleus core and electron shell. This sort of atomic-shell-like structure occurs also in ligand protected gold nanoparticles in which the gold core is positively charged and ligands are negatively charged, and leads to the stability of the gold-ligand complex.[42] An interesting

conclusion for the core-shell structure of Fe-Au nanoparticle is thus that the Au shell may prevent the Fe core from electrostatic interaction with outer species thus increasing the stability of the Fe-Au core.[16] Moreover, in view of catalysis and functionalization, extra electrons at the Au surface could be used to activate molecules or improve the binding of chemical functional groups, thus enhancing the catalytic activity and functionalization capacity of the Au surface.

d. Magnetic moment of bimetallic Fe_xAu_{113-x} (x=23, 56, 90)

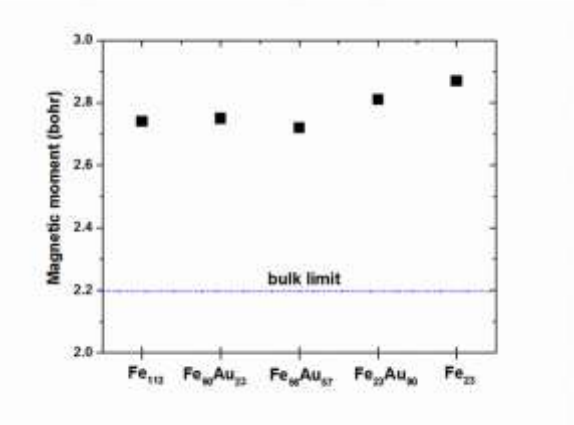

Figure 8. Magnetic moments of $Fe_{113-x}Au_x$ (x=23, 56, 90) and pure Fe_{113} and Fe_{23} nanoparticles.

Figure 8 shows the average magnetic moment (per Fe atom) for Fe-Au and pure Fe nanoparticles. First of all, in agreement with previous studies[11,16,22], regardless of Fe content, the Fe core maintains almost constant magnetic moment of ~2.8, which is 27% enhancement from the bulk value. In fact, the variation in the average magnetic moments shown in Fig. 8 is in accord with the variation in the size of Fe core of the nanoparticles with exception of $Fe_{56}Au_{57}$. That is, the smaller the size, the larger the magnetic moment. Difference between the highest (pure Fe_{23}) and the lowest magnetic moment ($Fe_{56}Au_{57}$) is $0.15\mu_B$. Secondly, the complete core-shell ($Fe_{56}Au_{57}$ and $Fe_{23}Au_{90}$) and partial core-shell structure ($Fe_{90}Au_{23}$) structures do not reduce the induced magnetic moment by a noticeable amount; By comparing the magnetic moment of $Fe_{23}Au_{90}$ and that of pure Fe_{23}, the reduction caused by the Au shell is only ~0.06 μ_B.

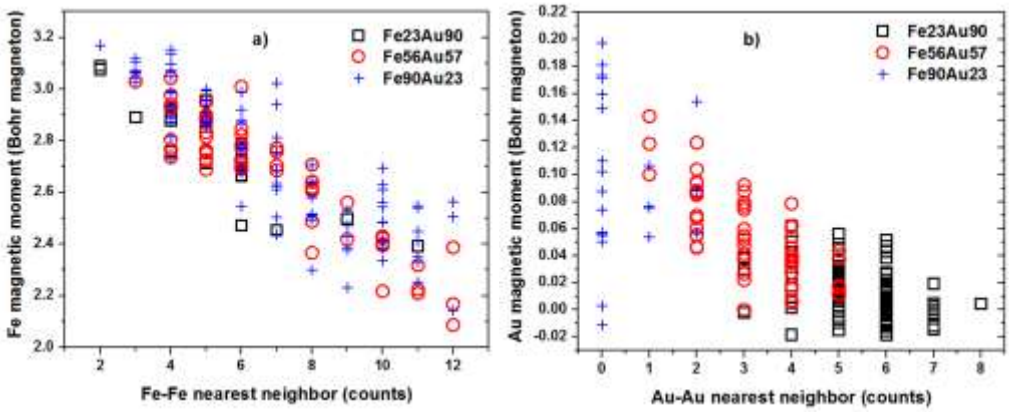

Figure 9. Distribution of magnetic moments of (a) Fe and (b) Au atoms over the local coordination in the Fe_xAu_{113-x} nanoparticles.

In fact, the magnetic moment of an Fe atom in the Fe-Au nanoparticles strongly depends on the local environment (Fig. 9). The local magnetic moment reveals insights into the Fe-Fe and Fe-Au interactions. First of all, the local magnetic moments of Fe atoms in all of the Fe-Au nanoparticles are all of the same sign, showing the magnetic coupling between Fe-Fe atoms are ferromagnetic (Fig. 9a) in agreement with previous studies[12,16]. However, when it comes to Au, different magnetic couplings between Au-Au atoms exist. Ferromagnetic coupling is observed for $Fe_{90}Au_{23}$ and $Fe_{56}Au_{57}$, but there exists antiferromagnetic coupling in $Fe_{23}Au_{90}$. Interestingly, all Au atoms (except one) that have negative magnetic moment are in the second Au layers although not all of the Au atoms in the second layer have negative magnetic moment (Fig. 10). Thus, the antiferromagnetic coupling occurs mostly between the 1st and 2nd Au layers. In all of the Fe-Au nanoparticles, the magnetic coupling between Fe and Au atoms are ferromagnetic.

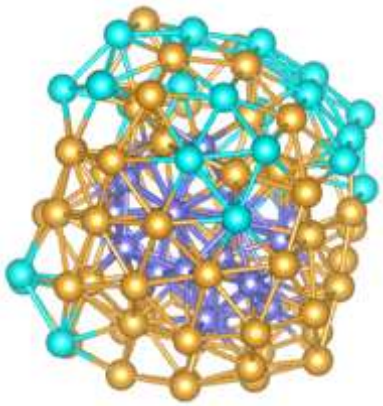

Figure 10. The magnetic ordering in $Fe_{23}Au_{90}$. Cyan represents the Au atoms with negative magnetic moment while brown the Au atoms with positive magnetic moment.

Thirdly, the local magnetic moment of Fe atoms are correlated with local coordination (Fig. 9a). Although there is deviation, the trend is such that the lower the Fe coordination, the larger the magnetic moment, and this trend is common for all Fe-Au nanoparticles. Note that as the Fe coordination approaches 11 the magnetic moment approaches about the bulk value ($2.2\mu_B$) (See Fig. 9a for $Fe_{90}Au_{23}$ in particular). The correlation is however not obvious for Au atoms, as the induced magnetic moments show large deviation (Fig. 9b).

The correlation of the local magnetic moment to the local environment is a result of charge transfer as demonstrated in Fig. 11a for Fe atoms. The more the depleted charge, the larger the magnetic moment (Fig. 11a). For Au, similarly but in the opposite sense, the more the acquired charge the larger the magnetic moment (Fig. 11b) but the deviation from this trend is large, particularly for Au atoms of $Fe_{56}Au_{57}$ nanoparticle. In fact, the magnetic moments that are deviated from the trend belong to those Au atoms that have the higher oxidation state of -0.55 and more, which seems to cause the reduction of the magnetic moment.

The correlation of the magnetic moment of the Fe atoms in the Fe-Au nanoparticles with the oxidation state indicates that electron depletion is crucial in the enhancement of the induced magnetic moment of the Fe atoms. As a matter of fact, the depleted electron originates from the spin-down state of the Fe atoms resulting in the enhanced magnetic moment of the Fe atoms near the shell (Fig. 7d).

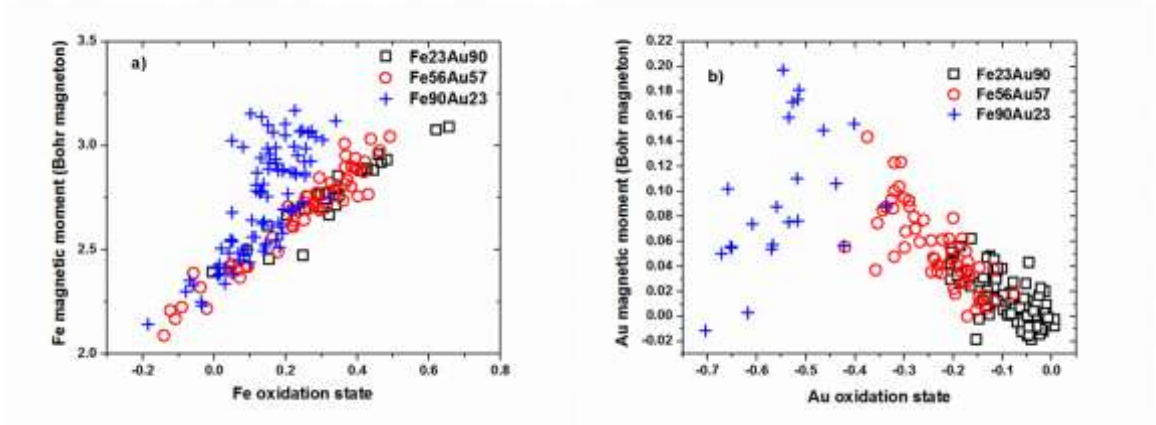

Figure 11. Correlation of magnetic moment with oxidation state. (A) Fe magnetic moment versus Fe oxidation state. (B) Au magnetic moment versus Au oxidation state.

4. Conclusions

Our calculations find that the Fe core of the Fe_xAu_{113-x} (x=23, 56, 90) nanoparticles maintains almost constant magnetic moment of ~2.8 regardless of Fe content, which is 27% enhancement from the bulk value in agreement with previous studies. The local magnetic moment of Fe atoms are correlated with the local coordination of Fe atoms and the enhanced magnetic moment is a result of charge depletion from Fe atoms to Au atoms. The more the depleted charge, the larger is the magnetic moment. This indicates that electron depletion is crucial in the enhancement of the induced magnetic moment for Fe atoms. Our calculations clearly show the formation of core-shell structure for Fe_xAu_{113-x} (x=23, 56, 90) nanoalloys although only a partial Au shell forms for $Fe_{90}Au_{23}$ owing to insufficient number of Au atoms in the cluster. This core-shell structure is more stable than the segregated phase consisting of two Fe and Au nanoparticles. Segregation between Fe and Au phases may be driven by large surface energy mismatch and core stress, but another important factor for the formation of the core-shell structure could be low surface tension in the Fe-Au interface (i.e., strong Fe-Au interfacial interaction), which we attribute to the large charge transfer at the interface.

Acknowledgement

We are grateful to Lyman Baker and Duy Le for careful reading of the manuscript and constructive comments. This work was supported in part by the Department of Energy, Basic Energy Sciences (DE-FG02-07ER46354). The DFT calculations were performed using the computing resources at Stokes in the Advanced Research Computing Center at University of Central Florida, at Carbon in Center for Nanoscale Materials at Argonne National Lab, at Hopper in National Energy Research Scientific Computing Center, and in Stampede at Text Advanced Computing Center.

Reference

(1) Mornet, S.; Vasseur, S.; Grasset, F.; Duguet, E. *Journal of Materials Chemistry* **2004**, *14*, 2161.

(2) Pankhurst, Q. A.; Connolly, J.; Jones, S. K.; Dobson, J. *Journal of Physics D: Applied Physics* **2003**, *36*, R167.

(3) Pedro, T.; María del Puerto, M.; Sabino, V.-V.; Teresita, G.-C.; Carlos, J. S. *Journal of Physics D: Applied Physics* **2003**, *36*, R182.

(4) Molenbroek, A. M.; Nørskov, J. K.; Clausen, B. S. *The Journal of Physical Chemistry B* **2001**, *105*, 5450.

(5) Chiang, I. C.; Chen, D. H. *Advanced Functional Materials* **2007**, *17*, 1311.

(6) Ravel, B.; Carpenter, E. E.; Harris, V. G. *Journal of Applied Physics* **2002**, *91*, 8195.

(7) Kinoshita, T.; Seino, S.; Okitsu, K.; Nakayama, T.; Nakagawa, T.; Yamamoto, T. A. *Journal of Alloys and Compounds* **2003**, *359*, 46.

(8) Ruban, A. V.; Skriver, H. L.; Nørskov, J. K. *Physical Review B* **1999**, *59*, 15990.

(9) Peng, Z.; Yang, H. *Journal of Solid State Chemistry* **2008**, *181*, 1546.

(10) McGuire, T. R.; Aboaf, J. A.; Klokholm, E. *Journal of Applied Physics* **1981**, *52*, 2205.
(11) Felsch, W. *Z. G. Angew Physik* **1970**, *29*, 217.
(12) Cannella, V.; Mydosh, J. A.; Budnick, J. I. *Journal of Applied Physics* **1971**, *42*, 1689.
(13) Fuß, A.; Demokritov, S.; Grünberg, P.; Zinn, W. *Journal of Magnetism and Magnetic Materials* **1992**, *103*, L221.
(14) Fang, C. M.; de Groot, R. A.; Bischoff, M. M. J.; van Kempen, H. *Physical Review B* **1998**, *58*, 6772.
(15) Khmelevskyi, S.; Kudrnovský, J.; Gyorffy, B. L.; Mohn, P.; Drchal, V.; Weinberger, P. *Physical Review B* **2004**, *70*, 224432.
(16) Sun, Q.; Kandalam, A. K.; Wang, Q.; Jena, P.; Kawazoe, Y.; Marquez, M. *Physical Review B* **2006**, *73*, 134409.
(17) Saha, D. K.; Koga, K.; Takeo, H. *Eur. Phys. J. D* **1999**, *9*, 539.
(18) Jal, E.; Dąbrowski, M.; Tonnerre, J.-M.; Przybylski, M.; Grenier, S.; Jaouen, N.; Kirschner, J. *Physical Review B* **2013**, *87*, 224418.
(19) Naitabdi, A.; Ono, L. K.; Behafarid, F.; Cuenya, B. R. *The Journal of Physical Chemistry C* **2009**, *113*, 1433.
(20) Cuenya, B. R.; Ono, L. K.; Croy, J. R.; Naitabdi, A.; Heinrich, H.; Zhao, J.; Alp, E. E.; Sturhahn, W.; Keune, W. *Applied Physics Letters* **2009**, *95*, 143103.
(21) HongLing, L.; Peng, H.; WengXing, Z.; Young Keun, K.; JunHua, W. *Nanotechnology* **2010**, *21*, 335602.
(22) Billas, I.; Becker, J.; Châtelain, A.; de Heer, W. *Physical Review Letters* **1993**, *71*, 4067.
(23) Hohenberg, P.; Kohn, W. *Phys Rev* **1964**, *136*, B864.
(24) Kohn, W.; Sham, L. J. *Phys Rev* **1965**, *140*, A1133.
(25) Kresse, G.; Furthmüller, J. *Phys. Rev. B* **1996**, *54*, 11169.
(26) Kresse, G.; Furthmüller, J. *Computational Materials Science* **1996**, *6*, 15.
(27) Kresse, G.; Hafner, J. *Physical Review B* **1993**, *47*, 558.
(28) Blöchl, P. E. *Phys. Rev. B* **1994**, *50*, 17953.
(29) Perdew, J. P.; Burke, K.; Ernzerhof, M. *Physical Review Letters* **1996**, *77*, 3865.
(30) Plimpton, S. *Journal of Computational Physics* **1995**, *117*, 1.
(31) Zhou, X. W.; Johnson, R. A.; Wadley, H. N. G. *Physical Review B* **2004**, *69*, 144113.
(32) Bader, R. *Oxford University Press, New York* **1990**.
(33) Tang, W.; Sanville, E.; Henkelman, G. *Journal of Physics: Condensed Matter* **2009**, *21*, 084204.
(34) Bach, L. G.; Rafiqul Islam, M.; Kim, J. H.; Kim, H. G.; Lim, K. T. *Journal of Applied Polymer Science* **2012**, *124*, 4755.
(35) Bochicchio, D.; Ferrando, R. *Physical Review B* **2013**, *87*, 165435.
(36) Laasonen, K.; Panizon, E.; Bochicchio, D.; Ferrando, R. *The Journal of Physical Chemistry C* **2013**, *117*, 26405.
(37) Riccardo, F. *Journal of Physics: Condensed Matter* **2015**, *27*, 013003.
(38) Nanda, K. K.; Maisels, A.; Kruis, F. E.; Fissan, H.; Stappert, S. *Physical Review Letters* **2003**, *91*, 106102.
(39) Wang, G.; Van Hove, M. A.; Ross, P. N.; Baskes, M. I. *Progress in Surface Science* **2005**, *79*, 28.
(40) Mottet, C.; Rossi, G.; Baletto, F.; Ferrando, R. *Physical Review Letters* **2005**, *95*, 035501.
(41) F. R. de Boer, R. B., W. C. M. Mattens, A. R. Miedema, and A. K. Niessen, Cohesion in Metals (North Holland, Amsterdam, 1988).
(42) Shafai, G.; Hong, S. Y.; Bertino, M.; Rahman, T. S. *Journal of Physical Chemistry C* **2009**, *113*, 12072.